Multichannel Imaging to Quantify Four Classes of Pharmacokinetic Distribution in Tumors

SUMIT BHATNAGAR,[1] EMILY DESCHENES,[1] JIANSHAN LIAO,[1] CORNELIUS CILLIERS,[1] GREG M. THURBER[1,2]

[1]Department of Chemical Engineering, University of Michigan, Ann Arbor, Michigan 48109
[2]Department of Biomedical Engineering, University of Michigan, Ann Arbor, Michigan 48109

ABSTRACT: Low and heterogeneous delivery of drugs and imaging agents to tumors results in decreased efficacy and poor imaging results. Systemic delivery involves a complex interplay of drug properties and physiological factors, and heterogeneity in the tumor microenvironment makes predicting and overcoming these limitations exceptionally difficult. Theoretical models have indicated that there are four different classes of pharmacokinetic behavior in tissue, depending on the fundamental steps in distribution. In order to study these limiting behaviors, we used multichannel fluorescence microscopy and stitching of high-resolution images to examine the distribution of four agents in the same tumor microenvironment. A validated generic partial differential equation model with a graphical user interface was used to select fluorescent agents exhibiting these four classes of behavior, and the imaging results agreed with predictions. BODIPY-FL exhibited higher concentrations in tissue with high blood flow, cetuximab gave perivascular distribution limited by permeability, high plasma protein and target binding resulted in diffusion-limited distribution for Hoechst 33342, and Integrisense 680 was limited by the number of binding sites in the tissue. Together, the probes and simulations can be used to investigate distribution in other tumor models, predict tumor drug distribution profiles, and design and interpret *in vivo* experiments. © 2014 Wiley Periodicals, Inc. and the American Pharmacists Association J Pharm Sci 103:3276–3286, 2014
Keywords: drug transport; imaging methods; in vivo/in vitro correlations (IVIVC); mathematical model; Krogh cylinder; fluorescence microscopy; predictive partial differential equation simulations

INTRODUCTION

Drug delivery and distribution in tumors is a complicated interplay of local tumor physiology and drug properties. Understanding and being able to predict this distribution is imperative to developing new therapies, as poor uptake has been shown to correlate with poor outcome in the clinic.[1] Tumor physiology is highly variable with gradients in oxygen,[2] metabolic waste products,[3] pH,[4] differences in extracellular matrix composition,[5,6] cell packing,[7] interstitial pressure,[8] multiple cell types,[9] poor blood flow,[10] increased and variable permeability,[11] and heterogeneous target concentrations[12] among others. For drug properties, the dose, molecular weight, charge,[13] target affinity and specificity, shape (e.g., globular versus linear macromolecules[14,15] or aspect ratio in nanoparticles[16]), surface chemistry (e.g., nanoparticles[17,18] and antibody drug conjugates[19]), lipophilicity,[20] pKa, local metabolism (e.g., antibody internalization), and systemic (plasma) clearance impact distribution. Even more complicated is that tissue physiology and drug property effects are not independent. Increasing dose may have little effect if a growth receptor is saturated,[21] for example, but have a major impact in another tumor or adjacent region with much higher receptor concentration where many receptors remain untargeted.

Tumor distribution is equally important for imaging agent development. Molecular imaging agents must reach their target to bind (e.g., radiolabeled ligands) or activate (e.g., protease sensors[22]) for accurate measurements. The physiochemical properties of the agent must allow the binding or activation to dominate distribution, otherwise nonspecific mechanisms such as membrane uptake may dictate the signal.[23] The requirements are even higher for quantitative imaging agents. Here, even if some of the target is exposed to the imaging agent, the resulting image may not be correlated with the amount of target.[24–28] In many cases, the imaging time will have an impact on the signal, such as fluorodeoxyglucose (FDG) that is limited by blood flow at early times[29] and glucose uptake and metabolism at later times.[30]

Because of the complex interplay of factors determining distribution, often multiple animal experiments are conducted with a variety of agents and variable results. This method is time consuming and expensive, with no guarantee that the models will mimic the clinical scenario. Mathematical simulations are playing a larger role in determining local distribution[31–34]; these models are capable of clearly identifying the impact of various factors (e.g., drug lipophilicity, tumor blood flow) on drug distribution using a fraction of the time and cost of experimental investigations. Predictive physiologically based pharmacokinetic (PBPK) models are increasingly able to determine the organ level distribution for small molecules[35–38] and biologics,[39–41] and these methods are useful for predicting the distribution in the clinic. However, assumptions that are valid in healthy tissue may fail in the tumor microenvironment. We have been developing partial differential equation (PDE) models to accurately describe the distribution of molecules in tumors.[31,42]

Correspondence to: Greg M. Thurber (Telephone: +734-764-8722; Fax: +734-763-0459; E-mail: gthurber@umich.edu)

Theoretical studies indicate that there are four major classes of pharmacokinetic distribution in tumors depending on the rate limiting step in uptake.[42] Molecules can be classified by (1) blood flow limitations, (2) extravasation limitations, (3) diffusion limitations, or (4) local binding and/or metabolism limitations, and these categories can be determined from the agent and tissue properties.[42] These classes are useful because they allow predictions about the impact of tumor physiology on distribution. For example, changes in macromolecular permeability would have no direct impact on a blood flow limited agent but a major change in an extravasation-limited agent.

Here, we use multichannel imaging within the same tumor to look at different patterns of distribution. The variability within and between tumors makes it difficult to parse out the impact of drug properties versus the local microenvironment. Using multichannel imaging, several drugs and imaging agents can be examined simultaneously in the same tumor to mitigate tumor microenvironment effects. The PDE model was used to predict the distribution of four molecules that displayed characteristics of the different classes of pharmacokinetic distribution. The selection criteria also ensured that these agents had different fluorescence excitation and emission profiles so they could be independently followed within the tumors. The model was also used to determine the imaging time after injection, and image analysis was performed to quantitatively compare the distribution with predictions.

BODIPY-FL was chosen as a representative blood flow limited molecule due to its low molecular weight and relatively low plasma protein binding for a fluorophore. Cetuximab is a chimeric monoclonal antibody used in the clinic to treat colon[43] and head and neck cancer[44]; it was selected as a representative antibody, which are generally limited by extravasation.[45] Hoechst 33258 was initially discovered and developed as an antiparasitic drug,[46] but both Hoechst dyes were quickly adopted for fluorescence imaging given their cell permeability and bright nuclear signal. Hoechst 33342 has been used in tumors to track functional vessels,[47,48] and its high plasma protein binding "buffers" the concentration within vessels so it is not depleted along the length of a tumor capillary. High cell uptake also allows it to quickly diffuse through endothelial cells, and the large number of DNA binding sites prevents it from saturating its target. Therefore, this agent is predicted to be limited by diffusion in the tissue. Hoechst 33258 has similar properties but is taken up by cells much slower than Hoechst 33342 even though they only differ by a hydroxyl versus an ethoxy group. Integrisense was originally developed as an $\alpha_v\beta_3$ integrin inhibitor for osteoporosis,[49] but high specificity and affinity for its target made it an excellent imaging agent after conjugation to a fluorophore.[50]

The distribution of these agents was studied in A-431 xenografts for several reasons. The high epidermal growth factor receptor (EGFR) expression in this line ($\sim$4 million receptors per cell) was predicted to give extravasation limited uptake for cetuximab (versus a saturating dose that would be limited by binding sites). The vasculature of this tumor is highly heterogeneous with some hypervascularized areas and other necrotic regions, replicating the variable tumor physiology seen in many animal models and the clinic. A-431 xenografts also have low $\alpha_v\beta_3$ expression ($\sim$10^4 receptors per cell[51]), ensuring that the Integrisense 680 imaging agent would saturate its target and therefore be binding site limited.

MATERIALS AND METHODS

Mathematical Model

The mathematical simulations were based on a previously published model.[42] Details can be found in the supplementary data (Section 1), but briefly, it consists of nonlinear PDEs with axial and radial gradients around a Krogh cylinder representation of tumor vessels. Time-dependent mixed boundary conditions determine the extravasation and depletion along the length of the vessel, and diffusion across a pseudo-homogeneous tissue with saturable binding and local metabolism dictates the tissue distribution. Equations are solved using finite differences in MATLAB (Mathworks), and a sparse Jacobian is specified to reduce computation time. Parameterization is also challenging with literature values often sparse and sometimes contradictory, especially for small molecules where equilibrium values are more readily available than kinetic rates. A table of parameters with references used in the predictions is listed in the supplementary data (Table S1, Supporting Information).

Cell Lines and Imaging Agents

A-431 cells were obtained from ATCC (Manassas, Virginia). Cetuximab (Bristol-Myers Squibb, Princeton, New Jersey) was conjugated with Alexa Fluor 750 (Life Technologies, Eugene, Oregon) according to the manufacturer's instructions. Briefly, 1.75 molar equivalents of dye were added to a solution of cetuximab (2 mg/mL) in 10% sodium bicarbonate and incubated at room temperature for 1 h. The conjugate was purified using 800 μL of 5 g/50 mL water of Biogel P-6 gel, Fine (Bio-Rad, Hercules, California; Cat. No. 150–4134) in Spin-X centrifuge filter tubes (Corning, Corning, New York; Cat. No. 8160) with a final degree of labeling of 1.4 dyes/antibody. Polyacrylamide gel electrophoresis was used to verify no free dye remained after purification. Anti-mouse CD31 (Biolegends, San Diego, California; Cat. No. 102402) and anti-EGFR (R&D Systems, Minneapolis, Minnesota; Cat. No. AF231) antibodies were labeled with Alexa Fluor 555 (Life Technologies) in a similar manner except the molar ratio was 5 instead of 1.75 for a higher degree of labeling as these antibodies were not injected *in vivo*. Integrisense 680 (PerkinElmer, Waltham, Massachusetts), Hoechst 33342, Hoechst 33258, and BODIPY-FL propionic acid (Invitrogen, Grand Island, New York) were used without further purification.

Plasma protein binding of Integrisense 680, Hoechst 33342 and 33258, and BODIPY-FL propionic acid were measured using a Rapid Equilibrium Dialysis (Thermo Scientific, Rockford, Illinois) plate according to the manufacturer's instructions. Mouse plasma (Innovative Research, Novi, Michigan; Cat. No. C57BL6) was mixed with either 20 μM of BODIPY FL, 50 μM of Hoechst dye, or 1 μM of Integrisense 680. After equilibration, the buffer in each chamber was adjusted to 50/50 mouse plasma and PBS to eliminate effects of protein binding on fluorescence. The signal was measured using either a SpectraMax M5 Microplate reader (Molecular Devices, Sunnyvale, California) or Odyssey CLx (Licor, Lincoln, Nebraska).

In Vitro Experiments

To measure the cellular uptake rate of Hoechst dyes in the presence of serum and at 37°C, A-431 cells were plated overnight in 96-well plates. Hoechst dyes were diluted with L-15 media

(without phenol red) and 10% FBS to concentrations of 10 and 100 µg/mL each. A microplate reader maintained at 37°C was used to measure fluorescence (excitation 350 nm, emission 450 nm), and the signal was background subtracted using wells with no cells. Experiments were conducted in triplicate, averaging five wells each time.

The kinetic rates of cellular uptake were determined by using a two-compartment model to fit the experimental data (Fig. S1, Supporting Information). Details are in the supplementary data (Supplemental Section 1), but the probe was assumed to cross the plasma membrane by passive diffusion[52,53] into an intracellular compartment and then transport to the nucleus and bind the DNA. When combining with the PDE model, the intracellular probe was considered immobile.

In Vivo Experiments

A-431 cells were used to grow tumor xenografts in 8–12 week old female nu/nu mice (Jackson Laboratory, Bar Harbor, Maine). All experiments involving mice were conducted in compliance with the University of Michigan University Committee on Use and Care of Animals (UCUCA). The cells were harvested using Trypsin–EDTA (0.05%), resuspended in PBS at a concentration of 1.5 million cells/50 µL, and injected subcutaneously in each hind limb while the mouse ($n = 16$) was anesthetized using isoflurane at 2% and 1 L/min oxygen. When the longest axis of the tumor was 5–10 mm, 0.2 nmol of Cetuximab and 2 nmol of Integrisense 680 were injected intravenously 24 h before euthanizing the mouse. 15 mg/kg of Hoechst 33342 or 33258 and 50 nmol of Bodipy FL were injected 3 h before and 2 min before euthanizing, respectively. All injections were formulated in 100–150 µL of phosphate-buffered saline. The tumors were then resected along with the liver, snap frozen in optimal cutting temperature (OCT) compound using isopentane cooled with dry ice. The tumors and liver were sectioned into 6 µm slices on a cryostat.

Slides were imaged using an upright Olympus FV1200 confocal microscope equipped with 405, 488, 543, 633, and 750 nm laser lines. High-resolution images of the entire tumor were created by stitching together individual images taken with a 20× objective and a motorized stage. Because BODIPY-FL was the only drug not bound to a target, these slides were pretreated with ethyl-3-[3-dimethylaminopropyl] carbodiimide (EDC) (Sigma–Aldrich, St. Louis, Missouri) to minimize washout before imaging this channel. Seventy-five microliters of a 0.5 M solution of EDC in PBS was added to the tissue for 15 min followed by a 3 × 3 min wash with PBS.

For *ex vivo* labeling of EGFR, unfixed slides were incubated with 75 µL of a 20 nM solution of Alexa Fluor 555 conjugated anti-EGFR antibody at room temperature for 25 min followed by a 3 × 3 min wash with PBS. The anti-mouse CD31 antibody was imaged in a similar manner. For integrin staining, slides were incubated at room temperature for 25 min with 75 µL of a 20 nM solution of a primary anti-$\alpha_v\beta_3$ antibody (R&D Systems; Cat. No. MAB 3050), followed by a 3 × 3 min wash in PBS, 15 min incubation in 75 µL of a 40 nM solution of the secondary anti-rabbit-TRITC (Sigma–Aldrich; Cat. No. T6778), 3 × 3 min wash, and imaged. JACoP,[54] a plug-in in FIJI, was used to analyze the *in vivo* and *ex vivo* labeling and generate a Pearson correlation coefficient.

For quantitative image analysis, 5–10 regions of interest were drawn around areas of tumor or liver samples for injected and uninjected mice imaged with identical settings on a confocal microscope (to minimize tissue thickness artifacts). The average intensity of injected samples was first compared to the uninjected controls to ensure we could measure the signal above background (verified by T-test of $p < 0.05$ for all samples), and then the signal was background subtracted. The values of at least three animals were compared between tissue samples for the reported results. For the Pearson correlation coefficients, individual values were calculated for a minimum of five images from each tumor and averaged.

Plasma Clearance

Plasma clearance studies of the drugs were conducted on C57BL/6J mice (Jackson Laboratory). Hoechst 33258 (480 nmol), fluorescently labeled cetuximab (0.2 nmol), and BODIPY-FL propionic acid (50 nmol) were dissolved in 75 µL of PBS and injected intravenously via the tail vein. Samples were obtained retro-orbitally or from the saphenous vein using heparin coated capillary tubes. Ten microliters of the blood was mixed with 20 µL of PBS–EDTA and centrifuged to remove cells. Plasma was pipetted into a 384-well plate, and the signal was measured on the SpectraMax M5 plate reader for Hoechst 33342 (excitation 350 nm and emission 450 nm) and BODIPY-FL (excitation 500 nm, emission 515 nm) fluorescence or Licor Odyssey for cetuximab fluorescence in the 800 nm channel (Fig. S4, Supporting Information) with a dilution series and plasma-only samples for background subtraction and quantification.

RESULTS

Table 1 displays the experimentally measured properties of the drugs and imaging agents used in this study. The molecules display a wide range in pharmacokinetic parameters and spectrally distinct fluorescence to enable independent tracking within the same tumor microenvironment. BODIPY-FL, cetuximab, and Hoechst 33258 plasma clearance was measured, and Hoechst 33342[55] and Integrisense 680[50] values were taken from the literature. The majority of BODIPY-FL propionic acid is cleared from the blood within 5 min and does not bind to a specific target, so the agent was injected 2 min before excising the tumor to capture differences in blood flow. The BODIPY-FL dose distributed in a 1.4 mL plasma volume would give an initial concentration of 35 µM, but the measured concentration at 1 min was closer to 5 µM. This indicates that significant redistribution occurred during the first minute between the tail vein injection and retro-orbital blood sample. Fluorescently tagged cetuximab distributed similar to unlabeled cetuximab,[56,57] indicating that the low degree of labeling (average of 1.4 dyes/antibody) had little impact on the plasma clearance over 1 day.

For the mathematical simulations, the full Krogh cylinder model simulates individual vessels within a tumor with gradients around the vessel (radial direction) and along the length of the vessel (axial direction) (Fig. 1). In a tumor, slow blood flow depletes small molecules along the length of the vessel as seen with BODIPY-FL. The small size (<300 Da) and moderate lipophilicity (predicted log $P = 3$ and log $D = -1$) causes the molecule to distribute quickly in the radial direction. However, the local plasma concentration is quickly depleted resulting in low uptake. This is in contrast to liver tissue. Here, higher blood flow reduces depletion along the length of the vessel

Table 1. Physiochemical and Optical Properties of Drugs and Imaging Agents

|	Target	Molecular Weight (Da)	Ex/Em (nm)	Plasma Protein Binding (%)	Plasma Clearance (α Fraction, α Half-Life, β Half-Life)
Bodipy FL	None	292	502/511	89.7 ($\pm$3.8)	56.2% alpha 2.6 min 30.37 min
Cetuximab + AF 750	EGFR	~153,000	752/780	NA	58% alpha 3.0 h 70.3 h
Hoechst 33342	DNA	452	352/455	99.3 ($\pm$0.4)	99.5% alpha 2 min 1 h
Hoechst 33258	DNA	424	352/455	98.8 ($\pm$0.9)	98.7% alpha 1.3 min 3.0 h
Integrisense 680	Integrins ($\alpha_V\beta_3$)	1432	675/693	94.9 ($\pm$2.3)	92.3% alpha 6 min 3.5 h
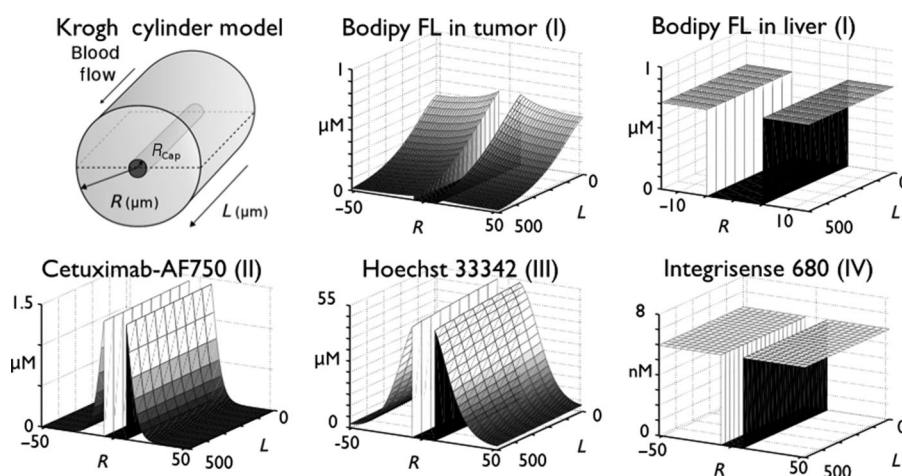
Figure 1. Simulations based on a Krogh cylinder model with axial and radial gradients (a). Four different agents were simulated with their predicted class of behavior show in parentheses. The results for BODIPY-FL in tumors (b) and liver (c) demonstrate axial blood flow limitations. The monoclonal antibody cetuximab has slow extravasation with rapid perivascular binding (d). The high plasma protein binding of Hoechst 33342 diminishes axial gradients, whereas slow diffusion into the tissue and rapid cellular uptake results in perivascular distribution (e). Integrisense 680 was simulated at a saturating dose, which results in no transport limitations and uptake equivalent to the receptor concentration (f).

giving much higher uptake (Fig. S5, Supporting Information). Antibodies such as cetuximab-AF750 have a permeability that is several orders of magnitude lower than small molecules, so the slow rate of extravasation does not deplete the concentration along the length of the vessel. Extravasation limits uptake, and the molecules that do reach the tissue quickly bind their target and are immobilized. This results in a perivascular distribution (Fig. 1). Hoechst 33342 also lacks a significant gradient along the length of the blood vessel. Although this is a small molecule like BODIPY-FL, it has much higher plasma protein binding. Binding to albumin and other proteins occurs on the millisecond time scale,[58] so as free drug extravasates, bound drug dissociates from proteins to replace it. Although 89.7% of BODIPY-FL propionic acid bound to plasma proteins versus 99.3% of Hoechst 33342 bound does not appear to be a large difference, it is the *free* drug that matters. The ratio of free drug (10.3% unbound BODIPY-FL versus 00.7% unbound Hoechst 33342) results in ~15-fold more free drug for BODIPY-FL. Like cetuximab, the large number of DNA binding sites per cell quickly immobilizes Hoechst 33342 before it diffuses deep

in the tissue, resulting in a perivascular distribution. Finally, Integrisense 680 lacks both radial and axial gradients as it saturates its receptor. In the simulation, a constant receptor concentration is assumed. The large dose of Integrisense relative to the low (~10^4 receptors/cell) $\alpha_v\beta_3$ expression in A-431 cells saturates the receptor within 30 min. The simulations for the other agents are shown at the time of tumor excision (2 min for BODIPY-FL, 24 h for cetuximab, and 3 h for Hoechst 33342), but it is shown at saturation after 30 min for Integrisense. At longer times, this agent is internalized and trapped while it clears from the background.

To compare the simulation predictions with experimental results, the distribution of these same agents under the same conditions was measured in tumor xenografts. Macroscopic (stitched) images of the entire tumor were used to reconstruct the distribution of all four agents throughout the whole tumor (Fig. 2). The BODIPY-FL signal is 14.7 times higher in the liver than the tumor ($p < 0.005$, Fig. S5, Supporting Information). This is consistent with the model predictions where much higher blood flow rates occur in the liver.[39] Cetuximab
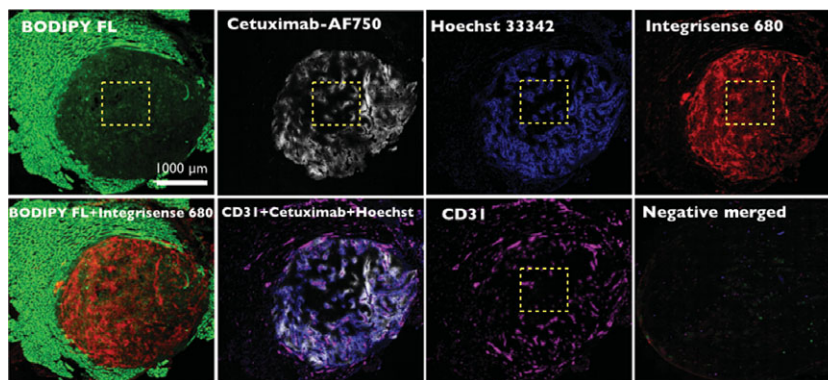
Figure 2. High-resolution multichannel fluorescence images were stitched together to generate a whole tumor image. BODIPY-FL and Integrisense 680 show more dispersed signal, whereas cetuximab-AF750 and Hoechst 33342 have a perivascular distribution in agreement with simulations. CD-31 staining was performed *ex vivo* to highlight all vessels. The uninjected negative control tumor is a merge of all five fluorescence channels. The yellow box corresponds to images in Figure 3.
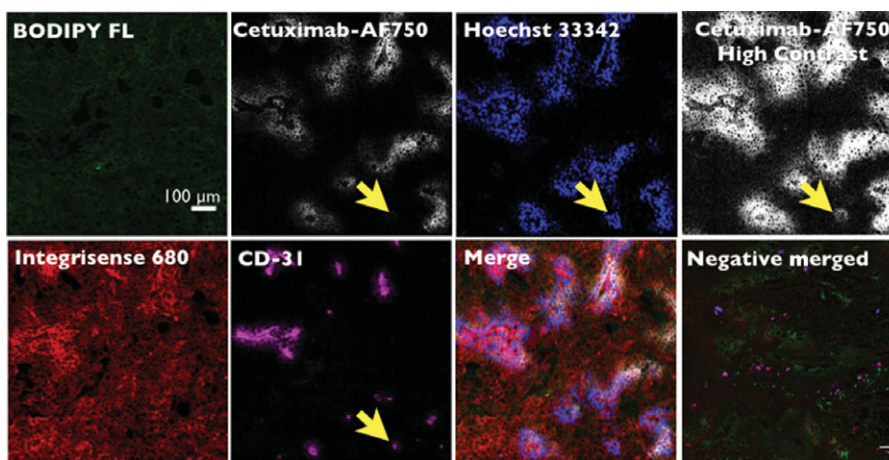

Figure 3. Cellular level imaging of the four fluorescent agents in a tumor corresponding to the box in Figure 2. The yellow arrows point to a vessel that causes prominent Hoechst 33342 staining but no apparent cetuximab staining. Perivascular cetuximab signal was seen only after increasing the contrast.

demonstrates a perivascular distribution in the tumor and no detectable signal in muscle that lacks human EGFR. Hoechst 33342 also exhibits a perivascular distribution within the tumor and labels nuclei in the surrounding muscle. Integrisense 680 shows a more uniform signal throughout the tumor, although it is higher in areas composed of macrophages and lower but detectable on tumor cells (Fig. S9, Supporting Information). CD31 labeling of the slide with an AlexaFluor-555 labeled antibody shows vasculature throughout the tumor and surrounding muscle. The signal in all images was higher than autofluorescence from uninjected controls (Figs. 2 and 3 and Figs. S6, S7, and S8, Supporting Information). The cetuximab and Integrisense-680 signals in the liver were close to background, and the Hoechst 33342 signal, limited by large diffusion distances in the tumor, was uniformly bright in all nuclei with slightly higher intensity (∼two-fold), which is not unexpected given the short diffusion distances in liver (data not shown).

Zooming in from the whole tumor to individual vessels, the local heterogeneity is more apparent (Fig. 3). BODIPY-FL cannot be detected easily as it has low tumor uptake and rapidly distributes, resulting in diffuse signal. Although the background autofluorescence of uninjected controls is less than

the measured signal in all four channels, the autofluorescence is highest relative to the probes in the 488 nm channel. Both cetuximab and Hoechst 33342 show large gradients in signal around the vessels, with few but distinct examples of mismatch: both Hoechst 33342 signal without cetuximab (yellow arrow) and cetuximab signal without Hoechst 33342 (data not shown). Integrisense 680 shows a more diffuse fluorescence consistent with saturated binding sites.

Hoechst 33342 uptake into cells is rapid, staining nuclei in seconds to minutes. Hoechst 33258, however, takes much longer to enter cells.[59] The nuclei reached saturation within 15 min with Hoechst 33342 but required over 2 h in Hoechst 33258 (Fig. S2, Supporting Information). Rapid cell uptake is predicted to quickly immobilize Hoechst 33342 near vessels, which can be seen at the macroscopic and vessel level (Fig. 4). The slower cell uptake of Hoechst 33258 is predicted to yield a more homogeneous distribution as the drug diffuses farther into the tissue before entering cells and binding DNA. At 5 min after injection, the Hoechst 33258 has not had time to diffuse deeper into the tissue and exhibits the same perivascular staining as Hoechst 33342 (with lower intensity, Fig. S10, Supporting Information), but by 3 h the pattern changes. The overall tumor distribution and vessel level images
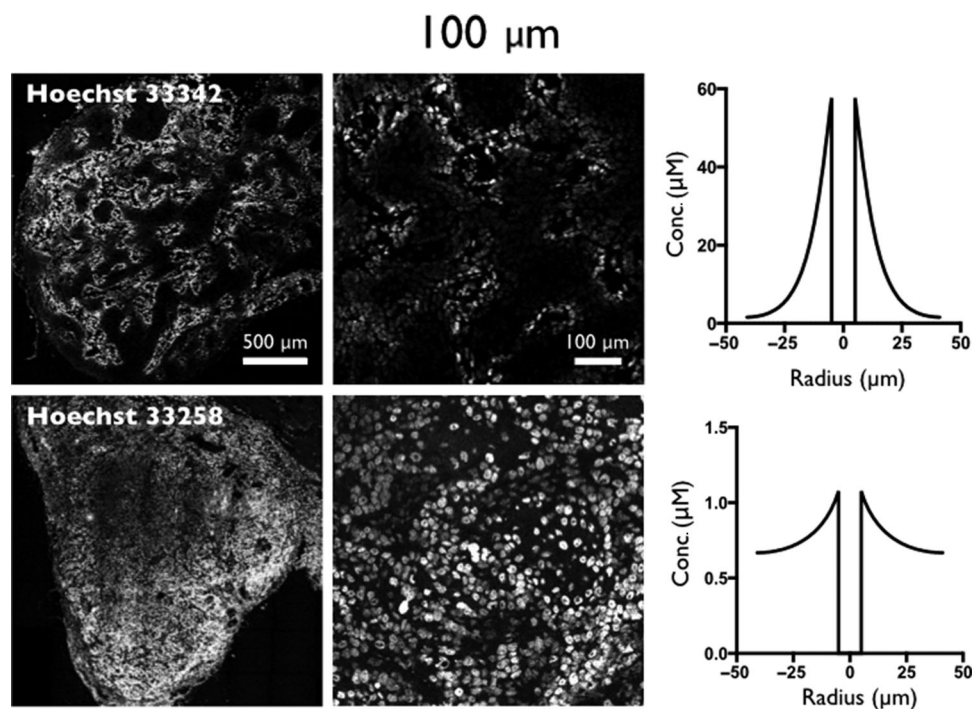
Figure 4. Images and simulations for Hoechst 33342 (top row) and Hoechst 33258 (bottom row). Macroscopic whole tumor images (left) show strong perivascular distribution of Hoechst 33342, whereas Hoechst 33258 displays a more even staining throughout the tumor. The signal intensity is much higher for Hoechst 33342 than Hoechst 33258, so the confocal settings and window leveling are different between the images. Higher resolution images (center) more clearly illustrate nuclear staining of perivascular cells for Hoechst 33342 with even staining for Hoechst 33258. Both dyes have a large increase in fluorescence when bound to DNA, so only the nuclear signal is apparent. Cellular uptake and binding rates were measured *in vitro* (Fig. S2, Supporting Information) and entered into the simulation. The radial plots predict rapid uptake and DNA binding relative to diffusion for Hoechst 33342 (top) versus cellular uptake slower than diffusion for Hoechst 33258 resulting in lower and more even concentrations.

capture this more uniform labeling, although the absolute signal intensity remains lower for Hoechst 33258 than Hoechst 33342.

Integrisense 680 has a more uniform but faint distribution throughout the tumor. In regions primarily consisting of A-431 cells, it has a reasonably high correlation coefficient with *ex vivo* anti-$\alpha_v\beta_3$ labeling (Fig. 5). However, there is also a significant signal in tumor macrophages. Based on estimates of pinocytosis in macrophages,[60] the signal in macrophages from fluid phase uptake is ∼70% higher than the low (∼10^4 receptors/cell) $\alpha_v\beta_3$-expression of A-431 cells. In addition, the Integrisense can bind to integrins on the macrophages.

The cetuximab staining shows a perivascular pattern when targeted *in vivo* (Fig. 5). *Ex vivo* labeling of the slide with a noncompetitive antibody shows significantly more EGFR farther from the vessels that was not targeted by the probe. The resulting Pearson correlation coefficient between these two images is lower as a result.

DISCUSSION

Drug distribution in tumors is difficult to study due to the heterogeneity in the physiology/tumor microenvironment combined with the effects of drug properties. The variability includes both intra- and intertumor tissue heterogeneity as well as temporal changes. To parse out the effect of drug properties on tumoral distribution, we used multichannel imaging within the same tumor to study the distribution of four different
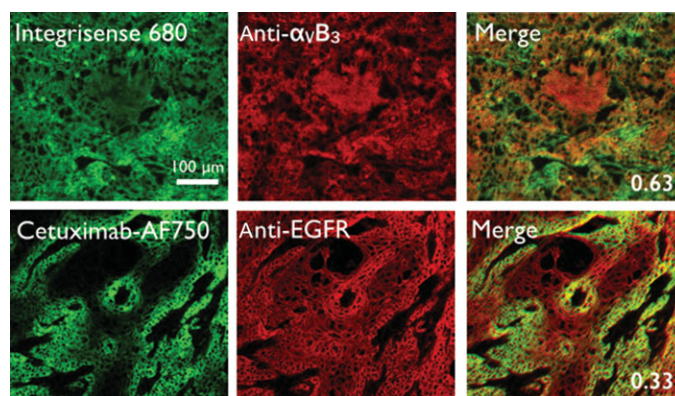

Figure 5. To conduct quantitative image analysis for a comparison with the simulations, tumor sections were labeled *ex vivo* with anti-$\alpha_v\beta_3$ (top middle) or anti-EGFR (bottom middle) AlexaFluor 555 antibody and compared with the *in vivo* signal (left). The Pearson correlation coefficient was high (0.63) for Integrisense 680, in agreement with the predicted saturating dose and lack of transport limitations. The correlation coefficient was lower (0.33) for cetuximab in agreement with predictions. The monoclonal antibody is limited by low permeability, and rapid binding immobilizes the high affinity antibody near the vessels. The Pearson correlation coefficients are based on average values for five regions within the tumor.

agents in the same tumor microenvironment. The imaging was paired with PDE simulations of these agents to compare the theoretical distribution with the experimental results. Overall, there was excellent agreement with the theoretical predictions

for all five simulated agents that varied in molecular weight, target specificity and expression, plasma clearance, and protein binding. The model is therefore capable of quickly and inexpensively investigating the impact of drug and tumor properties on distribution.

This PDE model predicts four broad classes of pharmacokinetic distribution in tumors (Fig. 1). By incorporating blood flow, extravasation, diffusion, and local binding and metabolism, a wide range of agents can be simulated and compared. This is in contrast to many models that make simplifying assumptions that limit the type of molecule that can be examined. By incorporating all the major steps in delivery to the tissue, the simulations are much more broadly applicable, and no simplifying assumptions need to be made *a priori*.[42] The first class is blood flow limited agents. This class includes many small molecules that have low plasma protein binding, so they have a large free fraction that rapidly extravasates across the vessel wall and quickly diffuses through the tissue (no diffusion limitations). Examples of this type of agent include many small molecules in healthy tissue.[35] Here, the nonspecific uptake is based on lipophilic distribution in the tissue. This is linear with drug log P values and tissue lipid content,[61] and therefore it never saturates (unlike class IV). The short diffusion distances result in few to no interstitial transport limitations (unlike class III), and the small size allows rapid extravasation (unlike class II). The result is that the agents are blood flow limited, and compartment models use this assumption in their development.[35]

Large molecules like biologics have limited extravasation between the endothelial cells, resulting in permeability limited uptake. This can be seen in validated models for biologics.[39,40,45] Here, compartmental models assume extravasation as the rate-limiting step, and these models focus on exchange between the tissue and vascular system based on convective and diffusive mechanisms. For tumors, elevated interstitial pressure results in diffusive uptake being the dominant mechanism,[62,63] but healthy tissue has significant convective extravasation and lymphatic drainage.[64] The heterogeneity often seen with antibodies can be captured with this PDE model. The heterogeneity results from rapid binding relative to interstitial transport (diffusion) and not directly because of low permeability. Cetuximab rapidly binds to the millions of receptors on the A-431 cells before it can diffuse away from the vessel. Only after the cells adjacent to the vessel are saturated do the antibodies diffuse deeper into the tissue. Internalization and metabolism by these cells may permanently prevent this from occurring.[65] Lower affinity antibodies can dissociate and diffuse farther in the tissue resulting in more homogeneous distribution,[66,67] although the rate-limiting step in uptake is still extravasation.

Diffusion limited drugs are often the least reported in the literature. These agents cannot be easily simulated with compartmental models due to the spatial gradients that develop in the tissue.[68] A typical class III agent is a small molecule (that can extravasate quickly, unlike class II) with high plasma protein binding (which buffers the free drug concentration along the length of a capillary, preventing class I designation). It may also have a nonsaturable mechanism of localization (e.g., high uptake in membranes) or high target expression (DNA binding of Hoechst dyes), so it is not limited by binding or metabolism. Unlike other classes that may be either homogeneous or heterogeneous in tissue, this molecule will display spatial gradients within the tissue.

The final class of agent, class IV or binding and metabolism-limited agents, cannot be generalized based on their physiochemical properties and can encompass small molecules and macromolecules with widely varying properties. These agents saturate their binding sites with additional probe that lacks free target to engage (or enzyme for activation[60]). With no more targets (binding site limited), the extra probe intravasates back into the blood. Because of this, the uptake in a particular tissue is correlated with the number of targets, which is ideal for imaging agents. For Integrisense, a low number of targets gave a low overall signal, and increasing the number of $\alpha_v\beta_3$ binding sites in the tissue results in much higher uptake in the tissue.[50] This intuitive result is not always the case for other agents such as antibodies.[24] Therefore, class IV agents are ideal for quantitative imaging.

Multichannel imaging allows the direct observation of distribution of multiple agents within the same tissue (Fig. 2). By stitching together images taken at high resolution, the pattern of uptake across the entire tumor could be reconstructed. Comparing different drugs in the same tissue, the differences can be directly attributed to drug properties and not variability in the tumor microenvironment, strengthening the conclusions. BODIPY-FL was chosen as a class I agent due to its small size, relatively low plasma protein binding (for a fluorophore), and green fluorescence which did not interfere with the other three agents. Blood flow rates to the liver are approximately fivefold to 10-fold higher than to tumors,[39,69,70] and this gives rise to hypoxia in A-431 tumors in particular.[71] The higher reported blood flow velocities in liver tissue (70–500 μm/s[72,73]) relative to tumors (20–200 μm/s[74]) resulted in higher predicted uptake in the liver than in the tumor, which is in agreement with our experimental observations. Cetuximab-AF750 extravasated from functional vessels and gave a perivascular pattern of uptake typical of high affinity biologics against highly expressed targets.[21,75,76] Hoechst 33342 has a high level of plasma protein binding (99.3%), so it fills the functional vessels within the tumor without significant depletion and has previously been used as a measure of perfused vessels.[47,48] This can be seen by comparing CD31 staining with Hoechst 33342 and cetuximab-AF750, where several CD31 stained vessels show a complete lack of Hoechst or cetuximab staining indicating the vessel had collapsed prior to injection of any of the agents. Integrisense 680 had staining throughout the tumor and lacked the perivascular pattern of cetuximab-AF750 and Hoechst 33342. The large dose injected relative to the low target expression ($\sim$10^4 receptors/cell) resulted in a saturation of the binding sites and a more even distribution. Experimentally, this group of agents could be used in conjunction with radiolabeled probes. By combining the fluorescent agents with autoradiography of an imaging agent or tritiated therapeutic, a comparison can be made between the new probe and the known fluorescent agents. This can help parse out the distribution of the radiolabeled agent due to target interaction versus the local tumor microenvironment.[77,78]

Using the high-magnification images, the pattern around individual vessels could be examined (Fig. 3). Within the tumor, little BODIPY-FL could be distinguished from background, although the average signal was statistically higher than negative (uninjected) control tumors ($p < 0.01$). Any probe entering the tumor quickly diffuses away from the vessel. Although we used a cross-linking agent to covalently fix the molecule to the tissue, some of the drug may have washed away before

it reacted. The liver uptake was high enough that even with these limitations, the signal was still statistically significantly higher than the tumor for this blood flow limited agent. The Integrisense 680 signal is much higher than background (due to target binding and lower autofluorescence in this channel) and stains cells throughout the tumor, both consistent with model predictions.

Comparing the cetuximab-AF750, Hoechst 33342, and CD31 staining, there are some CD31 vessels that stain for only cetuximab or Hoechst 33342. Unlike CD31 vessels that lack both probes and are likely collapsed, staining of only one compound shows that it was functioning at some point during the experiment. Transient blood flow in tumor vessels is a well-known phenomenon where the disrupted pressure gradients result in transient cessation and even reversal of flow.[79] Cetuximab-AF750 was injected 24 h prior to sacrifice, whereas Hoechst 33342 was injected 3 h beforehand. It is therefore not unexpected that some vessels would stain with the cetuximab-AF750 and then stop functioning at some point before the injection of Hoechst 33342. However, because the antibody is present the entire time Hoechst 33342 is in the blood, vessels that stain only with Hoechst 33342 are not expected. The likelihood of a vessel not functioning for the 21 h between the injections and then suddenly functioning for a few minutes after the Hoechst 33342 injection (where the majority of uptake occurs before its rapid clearance) is also low. This has been seen in other tumor models with trastuzumab and DIOC7 as a vascular stain.[75] This is unlikely, however, only if blood flow and the injections are independent events. The injection itself, either the probe or agents in the formulation, can alter blood pressure and tumor blood flow,[80] resulting in induced changes in blood flow patterns. If the contrast is increased on the cetuximab-AF750, there is staining around the vessels that initially appear to be stained only with Hoechst 33342 indicating that there was antibody in these vessels when they were delivering Hoechst 33342. Therefore, we hypothesize that the injection of Hoechst altered the tumor blood flow, resulting in these patterns and consistent with transient blood flow and model predictions.

Despite the established use of Hoechst 33342 to stain functional vessels in tumors, the kinetic rates of uptake have not been measured in much detail.[52,53] It has also been reported that the uptake of a very similar dye, Hoechst 33258, is much slower. However, reliable rates of cellular uptake have not been reported in the literature, and the distribution of Hoechst 33258 has not been analyzed *in vivo*. Different modes of binding and diffusion have been postulated for biologics and nanoparticles,[33,81] and we wanted to see if small molecules follow the same patterns. The modes include fast or slow binding and fast or slow dissociation. High-affinity antibodies exhibit fast association and slow release resulting in a binding site front or barrier,[82,83] and it appears Hoechst 33342 follows this pattern of quickly entering the cell, binding the target, and dissociating slowly. However, if Hoechst 33258 entered cells at a rate much slower than diffusion through the tissue, then it would distribute more homogeneously before entering the cells (effectively immobilized) and binding to the DNA. Given the lack of data in the literature, we quantified cellular uptake rates in A-431 cells for an accurate comparison. *In vitro* cell culture experiments showed saturation after 15 min with Hoechst 33342 versus 2 h with Hoechst 33258, and the modeling data indicated that the Hoechst 33258 would distribute more homogeneously (albeit at a lower concentration per cell, Fig. 4).

After injecting the same dose, this was exactly what was observed *in vivo*. We could not quantitatively compare the images as the intensity differences were too great to image both at the same microscopy settings. However, qualitatively, the pattern and intensity were consistent with predictions (Fig. 4). This example, where simply switching an ethoxy group to a hydroxyl group results in such a drastic change in distribution, is one reason why predictions based exclusively on structure (and no *in vitro* data) remain challenging. This also provides an example where modeling helps explain a counter-intuitive situation where rapid cell uptake results in poor distribution and poor cell uptake yields a more homogeneous distribution.

The modeling for the Hoechst dyes required a separate code to accurately simulate the distribution. The code used previously for antibodies[56] and small molecules[31,42] was based on a simplifying assumption for diffusion. Antibodies do not cross cell membranes, so diffusion occurs exclusively in the extracellular space, and the other small molecules crossed cell membranes fast enough to equilibrate between the intracellular and extracellular space relative to diffusion. The Hoechst dyes straddled these two extremes where the cellular uptake rate was on the same time-scale as diffusion in the tissue. Therefore, the cellular uptake rate had to be explicitly modeled in the equations (Fig. 4 and Supplemental Section 1).

For Integrisense 680, modeling predictions indicated the dose was much higher than necessary for saturation, and a low level of uptake was expected throughout the tumor. In regions primarily consisting of A-431 cells, the Pearson correlation coefficient between the intravenously delivered Integrisense-680 and its target (*ex vivo* stained $\alpha_v\beta_3$) is 0.63. This high correlation is expected for a receptor saturated with a probe.[65] However, in tumor macrophages detected with an anti-Mac3 antibody, the Integrisense 680 signal is slightly higher than on A-431 cells (Fig. S9, Supporting Information). Our initial hypothesis was that $\alpha_v\beta_3$ binding sites on activated macrophages[84] caused the higher uptake. However, a cross-reactive $\alpha_v\beta_3$ antibody (binding both human and mouse integrin) failed to stain these cells. Alternatively, we calculated whether fluid phase uptake would be sufficient for the higher macrophage signal. Although particle shape,[16] surface coatings,[85,86] and size[87,88] affect uptake, even PEGylated molecules that have low surface interaction are taken up by these cells.[22] Using a previous estimate of fluid phase uptake by macrophages,[60] the predicted concentration from nonspecific fluid phase uptake was twice that of the binding to A-431 cells. Therefore, we believe fluid phase uptake contributes to the higher macrophage than A-431 cell signal, but local binding or fluid phase uptake are both consistent with a lack of transport limitations and class 4 distribution.

Cetuximab-AF750 is limited by extravasation based on previous reports.[15,42] The dose used was sub-saturating, so for this high affinity antibody, only cells adjacent to blood vessels were labeled. This results in a lower Pearson correlation coefficient between intravenously delivered cetuximab and *ex vivo* ant-EGFR labeling. A larger dose would saturate all the binding sites[24] and result in a more homogeneous distribution (and higher Pearson correlation coefficient) as shown in tumor spheroids[65] and xenografts.[21,89]

One of the biggest hurdles to using mathematical models in research is the extensive effort required to develop a model and parameterize all the rates. Although software exists for compartmental models, the assumptions for these models are sometimes valid and other times inaccurate.[90] To facilitate the

use of this PDE model that does not have these limitations, we generated a graphical user interface (GUI) for the simulations (Fig. S3, Supporting Information). This allows a user to quickly simulate a wide range of agents, from small molecules to biologics and nanoparticles, without coding. The tumor physiology parameters can also be varied to study the impact on distribution in a matter of seconds, facilitating the use of the model for experimental predictions. This code can be used in designing experiments and interpreting *in vivo* data for new agents or tissues by modifying the parameters according to literature published values and correlations (Table S1, Supporting Information).

CONCLUSIONS

We have used multichannel imaging of four agents in a tumor and compared the distribution to a PDE model. The model distinguishes four different rate-limiting steps in uptake with practical applications such as imaging agent development or combination therapies that normalize the vasculature,[1,91] which may have synergistic or antagonistic effects. Together, a combined theoretical and experimental approach can help in designing more focused animal experiments, interpreting *in vivo* results, and developing improved therapeutics and imaging agents.

ACKNOWLEDGMENTS

REFERENCES

1. Goel S, Duda DG, Xu L, Munn LL, Boucher Y, Fukumura D, Jain RK. 2011. Normalization of the vasculature for treatment of cancer and other diseases. Physiol Rev 91(3):1071–1121.
2. Secomb TW, Hsu R, Park EYH, Dewhirst MW. 2004. Green's function methods for analysis of oxygen delivery to tissue by microvascular networks. Ann Biomed Eng 32(11):1519–1529.
3. Helmlinger G, Sckell A, Dellian M, Forbes N, Jain RK. 2002. Acid production in glycolysis-impaired tumors provides new insights into tumor metabolism. Clin Cancer Res 8:1284–1291.
4. Jain RK. 1999. Transport of molecules, particles, and cells in solid tumors. Annu Rev Biomed Eng 1:241–263.
5. Minchinton AI, Tannock IF. 2006. Drug penetration in solid tumours. Nat Rev Cancer 6(8):583–592.
6. Ohtani H. 1998. Stromal reaction in cancer tissue: Pathophysiologic significance of the expression of matrix-degrading enzymes in relation to matrix turnover and immune/inflammatory reactions. Pathol Int 48(1):1–9.
7. Grantab R, Sivananthan S, Tannock IF. 2006. The penetration of anticancer drugs through tumor tissue as a function of cellular adhesion and packing density of tumor cells. Cancer Res 66(2):1033–1039.
8. Baxter LT, Jain RK. 1989. Transport of fluid and macromolecules in tumors. I. Role of interstitial pressure and convection. Microvasc Res 37(1):77–104.
9. Karnoub AE, Dash AB, Vo AP, Sullivan A, Brooks MW, Bell GW, Richardson AL, Polyak K, Tubo R, Weinberg RA. 2007. Mesenchymal stem cells within tumour stroma promote breast cancer metastasis. Nature 449(7162):557–U554.
10. Jain RK, Ward-Hartley K. 1984. Tumor blood flow-characterization, modifications, and role in hyperthermia. IEEE Trans Sonics Ultrasonics 31(5):504–525.
11. Dreher MR, Liu W, Michelich CR, Dewhirst MW, Yuan F, Chilkoti A. 2006. Tumor vascular permeability, accumulation, and penetration of macromolecular drug carriers. J Natl Cancer Inst 98(5):335–344.
12. Kovtun YV, Audette CA, Ye Y, Xie H, Ruberti MF, Phinney SJ, Leece BA, Chittenden T, Blättler WA, Goldmacher VS. 2006. Antibody–drug conjugates designed to eradicate tumors with homogeneous and heterogeneous expression of the target antigen. Cancer Res 66(6):3214–3221.
13. Rosania GR, Lee JW, Ding L, Yoon HS, Chang YT. 2003. Combinatorial approach to organelle-targeted fluorescent library based on the styryl scaffold. J Am Chem Soc 125(5):1130–1131.
14. Dreher MR, Liu WG, Michelich CR, Dewhirst MW, Yuan F, Chilkoti A. 2006. Tumor vascular permeability, accumulation, and penetration of macromolecular drug carriers. J Natl Cancer Inst 98(5):335–344.
15. Gerlowski L, Jain RK. 1986. Microvascular permeability of normal and neoplastic tissues. Microvasc Res 31:288–305.
16. Champion JA, Mitragotri S. 2006. Role of target geometry in phagocytosis. Proc Natl Acad Sci USA 103(13):4930–4934.
17. Harris TJ, Green JJ, Fung PW, Langer R, Anderson DG, Bhatia SN. 2010. Tissue-specific gene delivery via nanoparticle coating. Biomaterials 31(5):998–1006.
18. Choi HS, Liu W, Liu F, Nasr K, Misra P, Bawendi MG, Frangioni JV. 2010. Design considerations for tumour-targeted nanoparticles. Nat Nanotechnol 5(1):42–47.
19. Hamblett KJ, Senter PD, Chace DF, Sun MM, Lenox J, Cerveny CG, Kissler KM, Bernhardt SX, Kopcha AK, Zabinski RF, Meyer DL, Francisco JA. 2004. Effects of drug loading on the antitumor activity of a monoclonal antibody drug conjugate. Clin Cancer Res 10(20):7063–7070.
20. Zhang X, Shedden K, Rosania GR. 2006. A cell-based molecular transport simulator for pharmacokinetic prediction and cheminformatic exploration. Mol Pharm 3(6):704–716.
21. Rhoden JJ, Wittrup KD. 2012. Dose dependence of intratumoral perivascular distribution of monoclonal antibodies. J Pharm Sci 101(2):860–867.
22. Weissleder R, Tung CH, Mahmood U, Bogdanov A. 1999. In vivo imaging of tumors with protease-activated near-infrared fluorescent probes. Nat Biotechnol 17(4):375–378.
23. Su H, Seimbille Y, Ferl GZ, Bodenstein C, Fueger B, Kim KJ, Hsu YT, Dubinett SM, Phelps ME, Czernin J, Weber WA. 2008. Evaluation of [F-18]gefitinib as a molecular imaging probe for the assessment of the epidermal growth factor receptor status in malignant tumors. Eur J Nucl Med Mol Imaging 35(6):1089–1099.
24. Thurber GM, Weissleder R. 2011. Quantitating antibody uptake in vivo: Conditional dependence on antigen expression levels. Mol Imaging Biol 13(4):623–632.
25. Cai WB, Chen K, He LN, Cao QH, Koong A, Chen XY. 2007. Quantitative PET of EGFR expression in xenograft-bearing mice using Cu-64-labeled cetuximab, a chimeric anti-EGFR monoclonal antibody. Eur J Nucl Med Mol Imaging 34(6):850–858.
26. McLarty K, Cornelissen B, Scollard DA, Done SJ, Chun K, Reilly RM. 2009. Associations between the uptake of In-111-DTPA-trastuzumab, HER2 density and response to trastuzumab (Herceptin) in athymic mice bearing subcutaneous human tumour xenografts. Eur J Nucl Med Mol Imaging 36(1):81–93.
27. Aerts H, Dubois L, Perk L, Vermaelen P, van Dongen G, Wouters BG, Lambin P. 2009. Disparity between in vivo EGFR expression and Zr-89-labeled cetuximab uptake assessed with PET. J Nucl Med 50(1):123–131.
28. Milenic DE, Wong KJ, Baidoo KE, Ray GL, Garmestani K, Williams M, Brechbiel MW. 2008. Cetuximab: Preclinical evaluation of a monoclonal antibody targeting EGFR for radioimmunodiagnostic and radioimmunotherapeutic applications. Cancer Biother Radiopharm 23(5):619–631.
29. Mullani NA, Herbst RS, O'Neil RG, Gould KL, Barron BJ, Abbruzzese JL. 2008. Tumor blood flow measured by PET dynamic imaging of first-pass F-18-FDG uptake: A comparison with O-15-labeled water-measured blood flow. J Nucl Med 49(4):517–523.

30. Patlak CS, Blasberg RG, Fenstermacher JD. 1983. Graphical evaluation of blood-to-brain transfer constants from multiple-time uptake data. J Cereb Blood Flow Metab 3(1):1–7.

31. Thurber GM, Yang KS, Reiner T, Kohler RH, Sorger P, Mitchison T, Weissleder R. 2013. Single-cell and subcellular pharmacokinetic imaging allows insight into drug action in vivo. Nat Commun 4:1504.

32. Venkatasubramanian R, Arenas RB, Henson MA, Forbes NS. 2010. Mechanistic modelling of dynamic MRI data predicts that tumour heterogeneity decreases therapeutic response. Br J Cancer 103(4):486–497.

33. Hauert S, Berman S, Nagpal R, Bhatia SN. 2013. A computational framework for identifying design guidelines to increase the penetration of targeted nanoparticles into tumors. Nano Today 8(6):566–576.

34. Wittrup KD, Thurber GM, Schmidt MM, Rhoden JJ. 2012. Practical theoretic guidance for the design of tumor-targeting agents. In: Methods in enzymology: Protein engineering for therapeutics; Wittrup KD, Verdine GL, Eds. Vol. 503. pp 255–268. Elsevier, Waltham, MA

35. Poulin P, Theil FP. 2002. Prediction of pharmacokinetics prior to in vivo studies. II. Generic physiologically based pharmacokinetic models of drug disposition. J Pharm Sci 91(5):1358–1370.

36. Peters SA. 2008. Evaluation of a generic physiologically based pharmacokinetic model for lineshape analysis. Clin Pharmacokinet 47(4):261–275.

37. Rowland M, Peck C, Tucker G. 2011. Physiologically-based pharmacokinetics in drug development and regulatory science. In: Annual review of pharmacology and toxicology; Cho AK, Ed. Vol. 51. Palo Alto: Annual Reviews, pp 45–73.

38. Rodgers T, Rowland M. 2007. Mechanistic approaches to volume of distribution predictions: Understanding the processes. Pharm Res 24(5):918–933.

39. Ferl GZ, Wu AM, DiStefano JJ. 2005. A predictive model of therapeutic monoclonal antibody dynamics and regulation by the neonatal fc receptor (FcRn). Ann Biomed Eng 33(11):1640–1652.

40. Garg A, Balthasar JP. 2007. Physiologically-based pharmacokinetic (PBPK) model to predict IgG tissue kinetics in wild-type and FcRn-knockout mice. J Pharmacokinet Pharmacodyn 34(5):687–709.

41. Mager DE. 2006. Quantitative structure-pharmacokinetic/pharmacodynamic relationships. Adv Drug Deliv Rev 58(12–13):1326–1356.

42. Thurber GM, Weissleder R. 2011. A systems approach for tumor pharmacokinetics. PLoS One 6(9).

43. Graham J, Muhsin M, Kirkpatrick P. 2004. Cetuximab. Nat Rev Drug Discov 3(7):549–550.

44. Astsaturov I, Cohen RB, Harari PM. 2006. EGFR-targeting monoclonal antibodies in head and neck cancer. Curr Cancer Drug Targets 6(8):691–710.

45. Thurber GM, Schmidt MM, Wittrup KD. 2008. Antibody tumor penetration: Transport opposed by systemic and antigen-mediated clearance. Adv Drug Deliv Rev 60(12):1421–1434.

46. Lammler G, Herzog H, Saupe E, Schutze HR. 1971. Chemotherapeutic studies on Litomosoides carinii infection of Mastomys natalensis. 1. The filaricidal action of 2,6-bis-benzimidazoles. Bull World Health Organ 44(6):751–756.

47. Chaplin DJ, Olive PL, Durand RE. 1987. Intermittent blood-flow in a murine tumor—Radiobiological effects. Cancer Res 47(2):597–601.

48. Trotter MJ, Chaplin DJ, Olive PL. 1989. Use of a carbocyanine dye as a marker of functional vasculature in murine tumors. Br J Cancer 59(5):706–709.

49. Coleman PJ, Brashear KM, Askew BC, Hutchinson JH, McVean CA, Duong LT, Feuston BP, Fernandez-Metzler C, Gentile MA, Hartman GD, Kimmel DB, Leu CT, Lipfert L, Merkle K, Pennypacker B, Prueksaritanont T, Rodan GA, Wesolowski GA, Rodan SB, Duggan ME. 2004. Nonpeptide alpha(v)beta(3) antagonists. Part 11: Discovery and preclinical evaluation of potent alpha v beta(3) antagonists for the prevention and treatment of osteoporosis. J Med Chem 47(20):4829–4837.

50. Kossodo S, Pickarski M, Lin S-A, Gleason A, Gaspar R, Buono C, Ho G, Blusztajn A, Cuneo G, Zhang J, Jensen J, Hargreaves R, Coleman P, Hartman G, Rajopadhye M, Duong LT, Sur C, Yared W, Peterson J, Bednar B. 2009. Dual in vivo quantification of integrin-targeted and protease-activated agents in cancer using fluorescence molecular tomography (FMT). Mol Imaging Biol 12(5):488–499.

51. Ferl GZ, Dumont RA, Hildebrandt IJ, Armijo A, Haubner R, Reischl G, Su H, Weber WA, Huang SC. 2009. Derivation of a compartmental model for quantifying Cu-64-DOTA-RGD kinetics in tumor-bearing mice. J Nucl Med 50(2):250–258.

52. Lalande ME, Ling V, Miller RG. 1981. Hoechst 33342 dye uptake as a probe of membrane permeability changes in mammalian cells. Proc Natl Acad Sci USA 78(1):363–367.

53. Grandjean TR, Chappell MJ, Yates JT, Jones K, Wood G, Coleman T. 2011. Compartmental modelling of the pharmacokinetics of a breast cancer resistance protein. Comput Methods Programs Biomed 104(2):81–92.

54. Bolte S, Cordelieres FP. 2006. A guided tour into subcellular colocalization analysis in light microscopy. J Micrsoopy 224:213–232.

55. Smith KA, Hill SA, Begg AC, Denekamp J. 1988. Validation of the Fluorescent Dye Hoechst 33342 as a vascular space marker in tumors. Br J Cancer 57(3):247–253.

56. Thurber GM, Zajic SC, Wittrup KD. 2007. Theoretic criteria for antibody penetration into solid tumors and micrometastases. J Nucl Med 48(6):995–999.

57. Oliveira S, Cohen R, Walsum MS, van Dongen GA, Elias SG, van Diest PJ, Mali W, van Bergen En, Henegouwen PM. 2012. A novel method to quantify IRDye800CW fluorescent antibody probes ex vivo in tissue distribution studies. EJNMMI Res 2(1):50.

58. Balaz S. 2009. Modeling kinetics of subcellular disposition of chemicals. Chem Rev 109:1793–1899.

59. Arndt-Jovin DJ, Jovin TM. 1977. Analysis and sorting of living cells according to deoxyribonucleic acid content. J Histochem Cytochem 25(7):585–589.

60. Thurber GM, Figueiredo JL, Weissleder R. 2009. Multicolor fluorescent intravital live microscopy (FILM) for surgical tumor resection in a mouse xenograft model. PLoS ONE 4(11):e8053.

61. Poulin P, Theil FP. 2000. A Priori prediction of tissue: Plasma partition coefficients of drugs to facilitate the use of physiologically-based pharmacokinetic models in drug discovery. J Pharm Sci 89(1):16–35.

62. Boucher Y, Baxter LT, Jain RK. 1990. Interstitial pressure-gradients in tissue-isolated and subcutaneous tumors—Implications for therapy. Cancer Res 50(15):4478–4484.

63. Jain RK, Baxter L. 1988. Mechanisms of heterogeneous distribution of monoclonal antibodies and other macromolecules in tumors: Significance of elevated interstitial pressure. Cancer Res 48:7022–7032.

64. Swartz MA. 2001. The physiology of the lymphatic system. Adv Drug Deliv Rev 50(1–2):3–20.

65. Thurber GM, Wittrup KD. 2008. Quantitative spatiotemporal analysis of antibody fragment diffusion and endocytic consumption in tumor spheroids. Cancer Res 68:3334–3341.

66. Adams G, Schier R, McCall A, Simmons H, Horak E, Alpaugh K, Marks J, Weiner L. 2001. High affinity restricts the localization and tumor penetration of single-chain Fv antibody molecules. Cancer Res 61:4750–4755.

67. Rudnick SI, Lou JL, Shaller CC, Tang Y, Klein-Szanto AJP, Weiner LM, Marks JD, Adams GP. 2011. Influence of affinity and antigen internalization on the uptake and penetration of anti-HER2 antibodies in solid tumors. Cancer Res 71(6):2250–2259.

68. Heijn M, Roberge S, Jain RK. 1999. Cellular membrane permeability of anthracyclines does not correlate with their delivery in a tissue-isolated tumor. Cancer Res 59(17):4458–4463.

69. Vaupel P, Kallinowski F, Okunieff P. 1989. Blood-flow, oxygen and nutrient supply, and metabolic microenvironment of human-tumors—A review. Cancer Res 49(23):6449–6465.

70. Baxter L, Zhu H, Mackensen D, Jain RK. 1994. Physiologically based pharmacokinetic model for specific and nonspecific monoclonal antibodies and fragments in normal tissues and human tumor xenografts in nude mice. Cancer Res 54:1517–1528.

71. Solomon B, Binns D, Roselt P, Weibe LI, McArthur GA, Cullinane C, Hicks RJ. 2005. Modulation of intratumoral hypoxia by the epidermal growth factor receptor inhibitor gefitinib detected using small animal PET imaging. Mol Cancer Ther 4(9):1417–1422.

72. Müller M, Keimling R, Lang S, Pauli J, Dahmen U, Dirsch O. 2009. Estimating blood flow velocity in liver vessels. In: Bildverarbeitung für die Medizin 2009; Meinzer H-P, Deserno T, Handels H, Tolxdorff T, Eds. Berlin Heidelberg: Springer, pp 36–40.

73. Sturesson C, Milstein DMJ, Post I, Maas AM, van Gulik TM. 2013. Laser speckle contrast imaging for assessment of liver microcirculation. Microvasc Res 87:34–40.

74. Jain RK. 1999. Transport of molecules, particles, and cells in solid tumors. Annu Rev Biomed Eng 01:241–263.

75. Baker J, Lindquist K, Huxham L, Kyle A, Sy J, Minchinton A. 2008. Direct visualization of heterogeneous extravascular distribution of trastuzumab in human epidermal growth factor receptor type 2 overexpressing xenografts. Clin Cancer Res 14(7):2171–2179.

76. Steffen AC, Orlova A, Wikman M, Nilsson FY, Stahl S, Adams GP, Tolmachev V, Carlsson J. 2006. Affibody-mediated tumour targeting of HER-2 expressing xenografts in mice. Eur J Nucl Med Mol Imaging 33(6):631–638.

77. Devaraj NK, Thurber GM, Keliher EJ, Marinelli B, Weissleder R. 2012. Reactive polymer enables efficient in vivo bioorthogonal chemistry. Proc Natl Acad Sci USA 109(13):4762–4767.

78. Keliher EJ, Reiner T, Thurber GM, Upadhyay R, Weissleder R. 2012. Efficient 18F-labeling of synthetic exendin-4 analogues for imaging beta cells. Chem Open1 (4): 177–183.

79. Baish JW, Netti PA, Jain RK. 1997. Transmural coupling of fluid flow in microcirculatory network and interstitium in tumors. Microvasc Res 53(2):128–141.

80. Trotter MJ, Olive PL, Chaplin DJ. 1990. Effect of vascular marker Hoechst-33342 on tumor perfusion and cardiovascular function in the mouse. 62(6):903–908.

81. Thurber G. 2011. Kinetics of antibody penetration into tumors. In: Targeted radionuclide therapy; Speer TW, Ed. Philadelphia: Lippincott Williams and Wilkins, pp 168–181.

82. van Osdol W, Fujimori K, Weinstein J. 1991. An analysis of monoclonal antibody distribution in microscopic tumor nodules: Consequences of a "Binding Site Barrier". Cancer Res 51:4776–4784.

83. Thurber G, Schmidt M, Wittrup KD. 2008. Factors determining antibody distribution in tumors. Trends Pharmacol Sci 29(2):57–61.

84. Huang S, Endo RI, Nemerow GR. 1995. Upregulation of integrins alpha v beta 3 and alpha v beta 5 on human monocytes and T lymphocytes facilitates adenovirus-mediated gene delivery. J Virol 69(4):2257–2263.

85. Perrault SD, Walkey C, Jennings T, Fischer HC, Chan WCW. 2009. Mediating tumor targeting efficiency of nanoparticles through design. Nano Lett 9(5):1909–1915.

86. Yang Z, Leon J, Martin M, Harder JW, Zhang R, Liang D, Lu W, Tian M, Gelovani JG, Qiao A, Li C. 2009. Pharmacokinetics and biodistribution of near-infrared fluorescence polymeric nanoparticles. Nanotechnology 20(16):11.

87. Choi HS, Ipe BI, Misra P, Lee JH, Bawendi MG, Frangioni JV. 2009. Tissue- and organ-selective biodistribution of NIR fluorescent quantum dots. Nano Lett 9(6):2354–2359.

88. Nahrendorf M, Waterman P, Thurber G, Groves K, Rajopadhye M, Panizzi P, Marinelli B, Aikawa E, Pittet MJ, Swirski FK, Weissleder R. 2009. Hybrid in vivo FMT-CT imaging of protease activity in atherosclerosis with customized nanosensors. Arterioscler Thromb Vasc Biol 29(10):1444–U1489.

89. Blumenthal RD, Fand I, Sharkey RM, Boerman OC, Kashi R, Goldenberg DM. 1991. The effect of antibody protein dose on the uniformity of tumor distribution of radioantibodies—An autoradiographic study. Cancer Immunol Immunother 33(6):351–358.

90. Thurber GM, Wittrup KD. 2012. A mechanistic compartmental model for total antibody uptake in tumors. J Theor Biol 314:57–68.

91. Jain RK. 2005. Normalization of tumor vasculature: An emerging concept in antiangiogenic therapy. Science 307(5706):58–62.